Power of a Quasispin Quantum Otto Engine at Negative Effective Spin Temperature

Jens Nettersheim,[1] Sabrina Burgardt,[1] Quentin Bouton,[1,2] Daniel Adam,[1] Eric Lutz[ORCID],[3] and Artur Widera[ORCID][1,*]

[1]*Department of Physics and Research Center OPTIMAS, Technische Universität Kaiserslautern, Kaiserslautern 67663, Germany*
[2]*Laboratoire de Physique des Lasers, CNRS, UMR 7538, Université Sorbonne Paris Nord, Villetaneuse F-93430, France*
[3]*Institute for Theoretical Physics I, University of Stuttgart, Stuttgart D-70550, Germany*

Heat engines usually operate by exchanging heat with thermal baths at different (positive) temperatures. Nonthermal baths may, however, lead to a significant performance boost. Here, we experimentally analyze the power output of a single-atom quantum Otto engine realized in the quasispin states of individual cesium atoms interacting with an atomic rubidium bath. From measured time-resolved populations of the quasispin state, we determine the dynamics during the cycle of both the effective spin temperature and of the quantum fluctuations of the engine, which we quantify with the help of the Shannon entropy. We find that power is enhanced in the negative-temperature regime and that it reaches its maximum value at half the maximum entropy. Quantitatively, operating our engine at negative effective temperatures increases the power by up to 30% compared to operation at positive temperatures, including the case of infinite temperature. At the same time, entering the negative-temperature regime allows for reducing the entropy to values close to zero, offering highly stable operation at high power output. We further numerically investigate the influence of the size of the Hilbert space on the performance of the quantum engine by varying the number of levels of the working medium. Our work thereby demonstrates control of a multilevel single-atom quantum engine interacting with a realistic atomic bath having many degrees of freedom.

I. INTRODUCTION

The capability of heat engines to produce mechanical work out of thermal energy has played a pivotal role in our society. They have been extensively utilized to generate motion, ranging from vehicles and ships to trains and airplanes [1]. Two central figures of merit of heat engines are efficiency, defined as the ratio of the work output and the heat input, and the power, which characterizes the work output rate. A large power output is essential from a practical point of view. Thermal machines with vanishing power indeed have limited application for transportation purposes, even if they have very high efficiency [1]. Macroscopic engines are commonly coupled to two (cold and hot) heat reservoirs that are used to modify the temperature of the working medium. Such large heat baths usually lead to thermal states with a positive temperature.

Technical development in past decades has led to a rapid miniaturization of thermal machines. The realization of both classical [2–9] and quantum [10–13] heat engines has been reported. These microscopic engines are frequently coupled to emulated reservoirs that can be easily controlled. As a result, they offer the possibility of preparing unconventional baths, such as coherent [14,15], squeezed [16,17], or negative-temperature [18] reservoirs. Remarkably, nonthermal baths have been predicted to enhance the performance of (classical and quantum) heat engines [14–20]. They can thus be considered as a useful thermodynamic resource. Recently, an efficiency boost has been experimentally demonstrated for a classical nanomechanical engine coupled to a simulated squeezed reservoir [17] and a quantum two-level engine interacting with an emulated bath at negative effective temperature in a nuclear magnetic resonance setup [18].

The study of negative temperatures has a long experimental [21–24] and theoretical [25–33] tradition, most prominently in nuclear magnetic resonance and atomic physics. They appear in systems with

---

*widera@physik.uni-kl.de

upper-bounded energy spectra and are associated with inverted states, known, for instance, from population inversion in laser physics [34]. They correspond to occupation probabilities that increase with the energy of the state—and not decrease with it, as is the case for thermal states with positive temperatures. Consequently, a system with a negative temperature is more energetic than one with a (positive) infinite temperature [35]. States with apparent negative temperatures may be interpreted as unstable nonequilibrium states that are consistent with the standard second law of thermodynamics [31]. The properties of heat engines coupled to baths at negative temperatures have been theoretically investigated in Refs. [36–40].

A fundamental limit of heat-engine operation is that of a single-atom motor, where the working medium consists of only one atom, instead of approximately 10^{25}, as is the case for macroscopic engines. Such a bound has been reached for classical [7–9] as well as for quantum [11–13] thermal machines. In these systems, the interaction with the heat reservoirs is often engineered, using, for instance, electrical noise [7], optical fields [8,9,11], or radio-frequency pulses [12]. The latter also applies to the recent notable study of the effect of negative effective temperatures on the efficiency of an elementary two-level quantum Otto engine [18]. Open issues in this context include the investigation of the influence of negative effective temperatures on (i) the power output (instead of the efficiency) of (ii) more complex many-level quantum heat engines (with finite Hilbert spaces) that are (iii) coupled to more realistic baths comprising many degrees of freedoms (which are more difficult to control), as well as (iv) the real-time monitoring of the population evolution of many-level single-atom working media. It is also worth noting that experimental realizations of negative effective temperatures have usually been performed in isolated quantum systems [21–24] and their implementation in an open quantum system interacting with a quantum reservoir consisting of an atomic gas is an interesting question.

In this paper, we experimentally investigate the occurrence of effective negative temperatures, and their enhancing effect on the power output, of a quantum Otto cycle consisting of a large quasispin (with $N = 7$ levels) of individual cesium (Cs) atoms collisionally coupled to an ultracold rubidium (Rb) gas, which plays the role of a quantum heat reservoir [13]. The latter environment may be regarded as a spin bath [41], where the relevant observables are the respective (internal) spin polarizations, instead of the (external) kinetic energies of the ultracold atoms. The time evolution [42–46] as well as the quantum thermodynamics [47–52] of systems interacting with a spin reservoir have been theoretically examined (see also the recent review on related quantum collisional models [53]). The angular-momentum transfer (spin transfer) between the system and the spin bath leads to an energy transfer

(spin energy transfer) between the two. From the point of the system, the spin energy transfer with the bath may be viewed as heat [51–53] (i.e., the energy exchange not being work). Owing to the finite Hilbert space of our $(N = 7)$-level quasispin, spin-exchange processes up (down) the energy ladder naturally stop when the upper (lower) energy level is reached. Assuming that the system starts in a positive-spin-temperature state (where lower energy levels are more populated than higher energy levels), a transition to negative spin temperature is achieved, when higher energy levels get more populated than lower energy levels.

Adiabatic expansion and compression phases of a quantum Otto cycle are implemented by modulating an external magnetic field that changes the energy-level spacing of the engine via the Zeeman effect and thus performs work [54]. Heat exchange between the system and the cold (hot) spin bath occurs via inelastic endoenergetic (exoenergetic) spin-exchange collisions [55]. We employ quantum control of the coherent spin-exchange process [56] to control the direction of heat transfer at the level of individual quanta and hence realize heating and cooling [54]. We additionally use single-atom and time-resolved measurements [57] of the quasispin distribution of a Cs atom to monitor the population dynamics of the engine along the cycle. As a result, we are able to follow the time evolution of both the effective spin temperature and the power output, and analyze their relationship. This allows us to gain a unique insight into the inner workings of a nanoscopic single-atom quantum heat engine.

The structure of the paper is as follows. We start in Sec. II by describing the experimental setup and the implementation of the quantum Otto cycle. In Sec. III, we analyze the population dynamics of the engine and determine the effective spin temperature during the cycle. We further investigate the quantum fluctuations of the system by evaluating the Shannon entropy of the spin distribution of the engine. In Sec. IV, we examine the time evolution of the power output and observe a power boost associated with the effective negative-temperature regime. Finally, in Sec. V, we compare the performance of our seven-level engine with that of an N-level machine.

II. EXPERIMENTAL SYSTEM

In our experiment, we immerse roughly a dozen Cs atoms into a bath of 10^4 Rb atoms at a kinetic temperature of approximately $T = 1$ μK—both species are confined in a common optical dipole trap [13], as illustrated in Fig. 1(a). The engine, which consists of an individual Cs atom, is realized in the seven hyperfine ground states of Cs, $|F_{Cs} = 3, m_{F,Cs}\rangle$, with the magnetic substates $m_{F,Cs} \in [+3, +2, \ldots, -3]$ (the lowest-energy state $m_{F,Cs} = 3$ marks the zero point). The bath of Rb atoms is prepared in the state $|F_{Rb} = 1, m_{F,Rb}\rangle$, with $m_{F,Rb} = \pm 1$. Spin-exchange collisions realize the heat transfer between

the engine and the bath, where in every collision the m_F state of the colliding Rb and Cs atoms is changed: a transition of the state of the engine by $\Delta m_{F,\text{Cs}} = -1$ (+1) corresponds to a directed energy transport where energy is absorbed (emitted) by the Cs atom. The strong atom-number imbalance of $N_{\text{Rb}}/N_{\text{Cs}} > 1000$ ensures that a bath atom collides only once with a Cs atom and is therefore transferred to $m_{F,\text{Rb}} = 0$; the bath can thus be considered as Markovian. Importantly, the engine is driven purely by the "spin fuel" of the Rb bath, while the kinetic temperature remains constant at all times. The effective spin temperature of this quantum bath is close to $T = \pm 0$ K, where the sign depends on the spin orientation. The bath therefore features a temperature range not accessible by usual thermal baths. During the engine cycle, the magnetic field B changes linearly between $B_1 = 346.5 \pm 0.2$ mG and $B_2 = 31.6 \pm 0.1$ mG in $\tau = 10$ ms. The Cs energy splitting at these magnetic fields is given by $E_n^{\text{Cs}} = n\lambda B$, with $n = 3 - m_{F,\text{Cs}}$ ($n \in 0, 1, \ldots, 6$ corresponding to $m_F \in 3, 2, \ldots, -3$) and $\lambda = |g_F^{\text{Cs}}|\mu_B$, where μ_B is the Bohr magneton and $g_F^{\text{Cs}} = -1/4$ is the Cs Landé factor. The amount of energy provided by a Rb atom during a spin-exchange collision is $\Delta E^{\text{Rb}} = \mp \kappa B$, with $\kappa = |g_F^{\text{Rb}}|\mu_B$, where $g_F^{\text{Rb}} = -1/2$ is the Rb Landé factor [55]. This value is twice the amount in the Cs spin system due to the twice larger Rb Landé factor. The spin-exchange collisions are thus inelastic. While each single collision is coherent and thus amenable to quantum state engineering, the coupling to the large number of bath modes in inelastic collisions destroys the coherence between the quasispin levels of the engine.

The quantum Otto cycle consists of four different branches [54]: adiabatic compression and expansion steps, during which work is performed, as well as isochoric heating and cooling stages, during which heat is exchanged [Fig. 1(b)]. Heat, $\langle Q \rangle = \sum_n E_n^{\text{Cs}} \Delta p_n$, is transferred between the engine and the bath via inelastic spin-exchange collisions, during heating (A → B) and cooling (C → D) strokes. Compression (D → A) and expansion (B → C) strokes, realized as adiabatic linear magnetic field changes, perform work, $\langle W \rangle = \sum_n p_n \Delta E_n^{\text{Cs}}$, where p_n is the Cs population in the nth m_F state. The cycle time is defined as $\tau_{\text{cycle}} = \tau_H + \tau_C + 2\tau$, where $\tau_{H,C}$ are the durations of the heating and cooling phases and 2τ is the combined duration of the adiabatic expansion and compression steps. The linear magnetic field ramps (of duration $\tau = 10$ ms each) are adiabatic with respect to the typical Zeeman splitting. At the same time, they are faster than the time scale on which spin-exchange processes occur (on average, 23 ms for a single spin-exchange event during heating and 42 ms for cooling). Thus, to a good approximation, no heat exchange takes place during expansion and compression strokes. Heat and work steps are accordingly well separated in the experiment, as they should be for an Otto cycle. The transition from a high-energy bath to a low-energy bath ($m_{F,\text{Rb}} = -1$ to $m_{F,\text{Rb}} = 1$) is realized
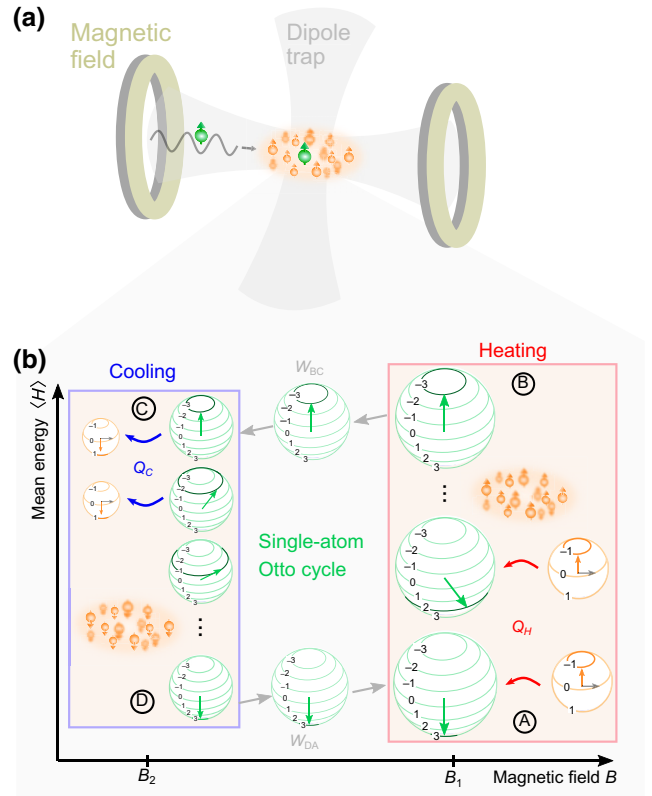

FIG. 1. The quasispin quantum Otto engine with the experimental setup. (a) The transport of a single Cs atom (green) into the ultracold Rb bath (orange) via an optical conveyor-belt lattice (sinuous line). Rb is trapped in an optical crossed-dipole trap, illustrated in gray. Magnetic field coils (yellow) control the magnetic environment. (b) The cycle of our quantum Otto heat engine is made up of four strokes: heating via spin-exchange collisions with the Rb bath (A → B), which provides heat $\langle Q_H \rangle$; compression by a linear magnetic field ramp (B → C), decreasing the energy-level splitting of the Cs atoms; cooling via spin-exchange collisions with the Rb bath (C → D), which extracts heat $\langle Q_C \rangle$; and compression by a second linear magnetic field ramp (D → A), which increases the energy-level splitting back to its initial value. In the figure, the m_F states are shown as level schemes of green (Cs) and orange (Rb) spheres. The gray arrows in the Rb spheres indicate the $m_F = 0$ state, which acts as the exhaust gas of our quantum heat engine.

via microwave sweeps that are more than one order of magnitude faster than the adiabatic magnetic field ramps [Fig. 1(b)]. In order to evaluate heat and work during the cycle, we determine the magnetic fields B_1 and B_2 with the help of Rb microwave spectroscopy [13]. We additionally detect the Zeeman populations p_n^i of individual Cs atoms at arbitrary times by position-resolved fluorescence measurements combined with Zeeman-state selective operations [57]. From a series of such measurements, we can, atom by atom, construct the quasispin populations at any time during the heat-engine cycle (Fig. 2, inset).
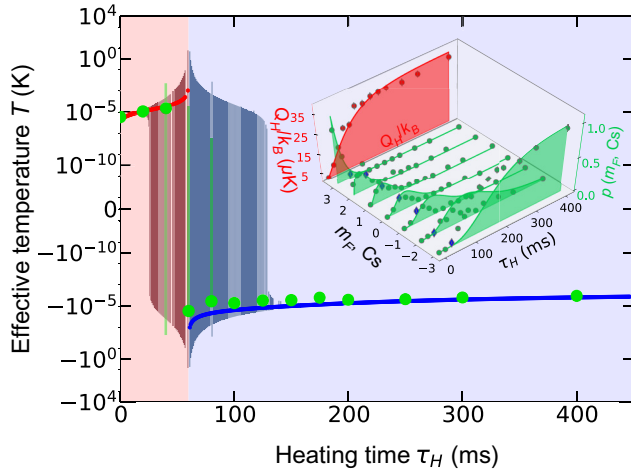
FIG. 2. The evolution of the effective spin temperature. By fitting the Cs population with $P_n = aP_+ + (1-a)P_-$ and Boltzmann distributions $P_\pm = \exp(-E_n^{Cs}/k_B T_\pm)/Z$, a positive (red) and negative (blue) temperature is extracted. The presented positive or negative temperature has a fit contribution of 98%. The large error bars indicate the transition area from positive to effective negative temperature. The green dots represent the extracted effective temperatures from measurements. The background colors indicate the positive (red) and negative (blue) effective temperature regimes. The inset shows the time evolution of the spin population p_n and of the exchanged heat Q_H of the heat engine reported in Ref. [13].

Our system possesses several unique features that distinguish it from other microscopic machines [2–12]. First, the engine spans seven quantum states exhibiting a natural stop of heat exchange if the highest- or lowest-energy state is populated. This is in marked contrast to unbound energy spectra such as harmonic oscillator systems. This property allows us to control the quantum fluctuations in the system, which are associated with random transitions between its discrete levels. Second, the quantum bath is realized by an ultracold atomic gas, where the spin polarization rather than the kinetic temperature stores the fuel of the engine. Controlling coherent collisional events, we can direct the heat exchange to either increase or decrease the spin energy of the engine in each spin-exchange collision. This aspect permits us to invert the spin population of the engine and achieve negative spin temperatures. Third, we can resolve the quantum-spin population time evolution at the level of individual quanta, yielding access to the mean but also to the fluctuations of the heat energy of the engine. This feature enables us to follow the dynamics of the heat engine throughout its cycle.

III. POPULATION DYNAMICS AND NEGATIVE SPIN TEMPERATURES

Combining quantum engineering of the spin states of both the machine and the environment, we can control the

energy transfer between the engine and the atomic bath at the level of single quanta. Starting from the lowest Cs energy level $|m_{F,Cs} = 3\rangle$, a maximum of six quanta can be stored in the machine after six spin-exchange collisions during heating, after which the system is in the highest Cs energy level $|m_{F,Cs} = -3\rangle$. Conversely, starting from the highest Cs energy level, a maximum of six quanta can be extracted from the machine after six spin-exchange collisions during cooling, after which the system is again in the lowest Cs energy level.

The population dynamics of the engine and the corresponding time-resolved heat transfer are shown in the inset of Fig. 2 for a typical heating phase. Starting from the lowest-energy spin-polarized state, spin-exchange collisions significantly broaden the distribution $p(m_{F,Cs})$ until after approximately three spin-exchange collisions a maximally broad distribution is reached. Further heat transfer leads to a reduction of the width of the distribution until the other state of extreme energy is reached. These population dynamics will significantly affect the effective spin temperature and the size of the quantum fluctuations in the system—and, in turn, the thermodynamic performance of the machine.

In order to quantify the effective spin temperature, we fit a sum of two Maxwell-Boltzmann distributions to the data, $P_n = aP_+ + (1-a)P_-$, one for positive (+) and the other one for negative (−) temperatures, with

$$P_\pm = \exp(-E_n^{Cs}/k_B T_\pm)/Z_\pm, \qquad (1)$$

where $Z_\pm$ is the partition function and $T_\pm$ is the effective positive or negative temperature (k_B is the Boltzmann constant). The amplitude a is a fit parameter that allows us to identify regimes of positive or negative temperatures or, for large uncertainty of a in a fit, the transition regime (for details, see Appendix A). The time evolution of the effective spin temperature is shown in Fig. 2 as a function of the heating time τ_H. For short interaction times, the data (green dots) are well reproduced by an effective positive temperature, which increases with the interaction time (the solid blue and red lines are simulations of a theoretical model; see Appendix B). The transition between positive and negative temperatures occurs at roughly 60 ms, when the spin distribution shows its greatest width. For longer interaction times, the system is well described by a negative effective temperature, indicating population inversion [34]. The largest amount of energy turnover during heating is reached for an initial (final) state with a very small effective temperature in the positive- (negative-) temperature domain.

The population dynamics impact the size of the quantum fluctuations in the system. Fluctuations vanish in the lowest- and highest-energy states since they are pure and increase for mixed states. We quantify the evolution of the width of the spin distribution of the engine, and thus of the

quantum fluctuations, by computing the Shannon entropy of the system during the heat-exchange process. From the measured population distribution of each m_F state at every time, the Shannon entropy is given by [35]

$$S = -k_B \sum_{m_F=+3}^{-3} p_{m_F} \ln p_{m_F}. \qquad (2)$$

Entropies have been extensively used to quantify the size of fluctuations, most notably in entropic uncertainty relations [58–60]. They have been shown to offer better bounds than those based on the variance [58–60]. Here, we employ Eq. (2) to quantify (i) the size of the quantum fluctuations [58–60] and (ii) the amount of information [35] stored in the engine.

The entropy dynamics are shown as a function of the cycle time, $\tau_{\text{cycle}} = \tau_H + \tau_C + 2\tau$, in Fig. 3(a), as a solid red line for the heating stage (A → B) [the expansion (compression) time τ is held constant and the heat (cooling) time is varied]. Here, the theoretical curves are obtained from numerical simulations of the heating process using the experimental parameters (for details of the spin-exchange model, see Appendix B). Starting from the lowest-energy zero-entropy state, the entropy increases as more engine-spin states are populated by spin-exchange collisions. The entropy passes a maximum, which is close to the theoretical maximum-entropy value for seven spin states of $S_{\text{max}} = k_B \ln 7$ at approximately 60 ms, until it approaches zero for longer interaction times. Interestingly, the entropy maximum (the largest quantum fluctuations or stored information) occurs at the time at which the effective temperature becomes negative (a similar behavior is known for the case of a two-level system [35]). At the end of a full heating step, the system is in the maximum-energy zero-entropy state and the subsequent cooling stroke starts with the polarized state $|m_{F,\text{Cs}} = -3\rangle$. However, the entropy evolution during the cooling stage (C → D) [the dashed colored lines in Fig. 3(a)] depends strongly on whether or not the maximum entropy point, located at $\tau_H = 58$ ms, has been reached. For short heating rates ($\tau_H \leq 58$ ms), the entropy decreases monotonically to zero—in this case, the entropy curve displays a single peak. For long heating rates ($\tau_H \geq 58$ ms), the entropy first increases and then reaches its maximum value, before decreasing again—in this case, the entropy curve exhibits a double-peak structure.

Both behaviors are observed experimentally [see Figs. 3(b) and 3(c)]. The data for full heating are represented by red dots and agree well with the simulated curve (deviations are due to experimental imperfections). For a short heating time ($\tau_H = 20$ ms) [the blue diamonds in Fig. 3(b)], the negative-temperature domain is not reached and the entropy decreases monotonically during cooling. By contrast, for a long heating time ($\tau_H = 300$ ms) [the
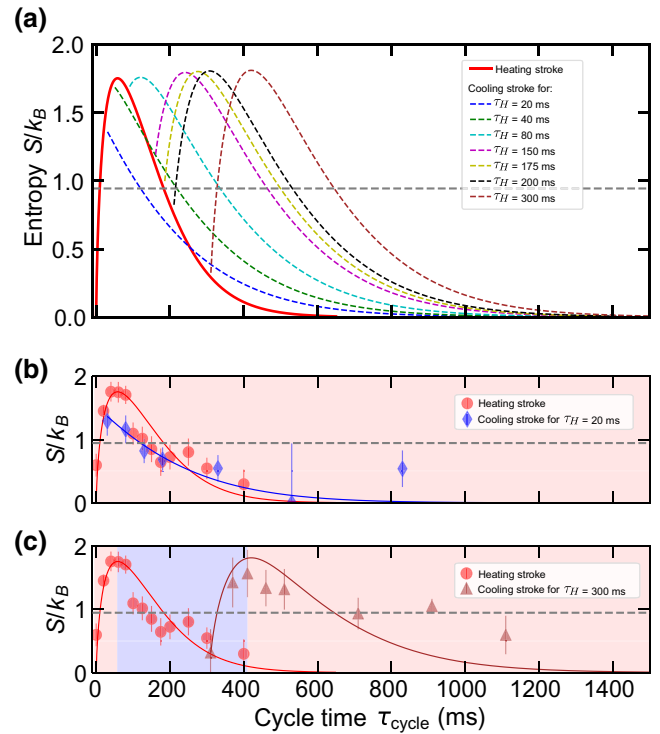

FIG. 3. The evolution of the Shannon entropy. (a) The Shannon entropy, given in Eq. (2), as a function of the cycle time τ_{cycle}: the behavior for the heating stroke A → B (red, solid) and for the cooling stroke C → D (other colors, dashed). The times in the legend indicate the heating time τ_H. The initial state $|m_{F,\text{Cs}} = +3\rangle$ is fully polarized (see Fig. 2) and leads to an initial zero entropy. Large heating times populate the system in $|m_{F,\text{Cs}} = -3\rangle$, giving a low entropy again. The maximum is reached for a mostly spread spin distribution, which is theoretically reachable for a population of 1/7 in each of the seven states. The population of highly excited states during heating leads to a second entropy maximum while cooling. Short heating times do not lead to the double-peak structure. (b) The evolution of the Shannon entropy for a short heating time $\tau_H = 20$ ms. The dots show the data for the heating stroke and the diamonds those for the cooling stroke. The solid lines are simulations based on our spin-exchange model. The horizontal dashed lines mark the entropy of cycle points B and C when the engine is running at full power. (c) The evolution of the Shannon entropy for a large heating time $\tau_H = 300$ ms. The dots show the data for the heating stroke and the triangles those for the cooling stroke. One can see that for the longer time, the system operates in the negative-temperature regime between the two entropy peaks, which is not crossed for the shorter time. Atomic losses cause deviations from the simulation for very large times.

brown triangles in Fig. 3(c)], the negative-temperature domain is reached (depicted by the blue-shaded area), and the entropy curve exhibits two distinct peaks. After reaching the second entropy peak, most atoms populate low energetic states and the engine enters the effective positive-temperature operation area, highlighted by the red

background. For very long interaction times, the measured entropy values deviate from the expected curve in Fig. 3(c). Here, the decrease of entropy expected from population accumulation in the extreme Zeeman state competes with the effect of Cs-atom losses via three-body recombination in the Rb gas. These losses tend to suppress the contrast of the population-distribution measurement, causing a reduced entropy signal. Additionally, due to experimental imperfections, a small background of, on average, 0.5 Cs atoms are equally distributed over all Zeeman states, not contributing to the exchange dynamics with the bath. Due to the atom losses, this background becomes increasingly relevant and therefore tends to increase the measured entropy.

IV. POWER ENHANCEMENT

We next analyze how negative spin temperatures and quantum fluctuations affect the power output of the engine. The efficiency η, defined as the ratio of the work output and the heat input, is constant, since driving is always adiabatic in our experiment [13]. As a result, nonadiabatic transitions do not occur during expansion and compression phases. The power output P is given by the work output $|\langle W \rangle| = \langle Q_H \rangle - |\langle Q_C \rangle|$ divided by the cycle time:

$$P = \frac{\langle Q_H \rangle - |\langle Q_C \rangle|}{\tau_{\text{cycle}}} = \frac{|\langle W \rangle|}{\tau_{\text{cycle}}}. \quad (3)$$

We experimentally evaluate P by measuring the spin-population changes during the heating stroke, $p_n(A \to B)$, and during the cooling stroke, $p_n(C \to D)$, from which we directly determine the energy exchanged during heating, $\langle Q_H \rangle = \sum_n E_n^{\text{Cs}}(B_1) \Delta p_n(A \to B)$, and during cooling, $\langle Q_C \rangle = \sum_n E_n^{\text{Cs}}(B_2) \Delta p_n(C \to D)$ (the values of the energy splitting, $E_n^{\text{Cs}}(B_1)$ and $E_n^{\text{Cs}}(B_2)$, are computed from the measured magnetic fields). We follow the evolution of the power output during the heat-engine cycle by plotting P as a function of the Shannon entropy S during the heating stroke, as shown in Fig. 4. It is sufficient to consider only the heating-stroke entropy of the engine, since the final heating-stroke entropy determines the initial cooling-stroke entropy (the compression step being unitary) and the Cs ground $|m_{F,\text{Cs}} = 3\rangle$ has to be reached on the cooling-stroke side to realize a cycle. The blue dots represent experimental data and the red line is the theoretical simulation. The numbered green dots indicate the number of spin-exchange collisions (associated with a transition from one discrete energy level to another). The engine starts from the lowest-energy state, where both the heating-stroke entropy and the power are low. For an increasing energy intake during the spin-exchange process, both the entropy and the power increase very similarly to the behavior of a standard thermal engine. The spin temperature is positive (the red-shaded area) until the
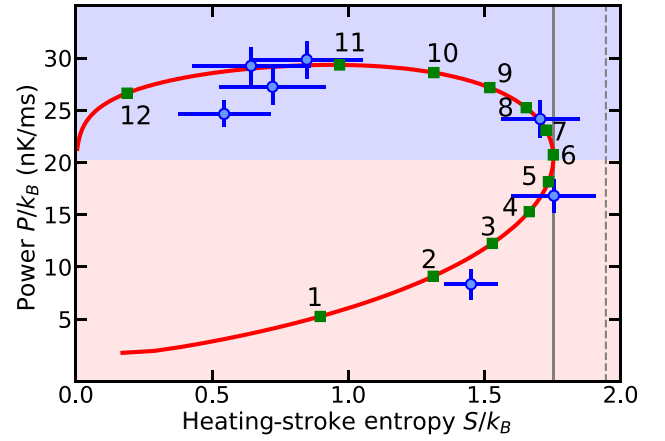

FIG. 4. The evolution of the power output. The blue dots represent the experimental data and the red line is the theoretical prediction based on our spin-exchange model. The green dots and associated numbers give the number of total spin-exchange collisions for a full cycle (collision number 12 is not located at the end of the red line due to numerical errors in calculating the total number of spin-exchange collisions of approximately 1%). The red area marks the positive-temperature regime and the blue denotes negative temperatures, when most atoms are populated in energetically higher states. The gray dashed vertical line indicates the theoretical entropy maximum ln(7) of the system and the solid vertical line the maximum entropy of the engine at 1.75. The maximum power output is reached at roughly half that value.

point of maximum entropy (i.e., maximum fluctuations), $S_{\text{max}}/k_B = 1.75 \approx \ln 7$, is reached after roughly six spin-exchange collisions. Subsequently, the engine operates in the effective negative-temperature regime (the blue-shaded area). Here, the Shannon entropy saturates and then starts decreasing, while the power output increases further, by roughly 30% compared to the case at maximum heat-stroke entropy. The maximum power of $P_{\text{max}} = k_B \times 30$ nK/ms is reached at roughly half the maximum entropy of $S/k_B \approx 0.9$, corresponding to 11 spin-exchange collisions during the cycle. This key physical insight is directly linked to the high degree of control of the spin polarizations of both the system and the bath in the experiment and our ability to monitor the time evolution of the spin population at the level of single-quanta, one spin-exchange collision at a time. The power decreases after P_{max}, since the work output saturates and the cycle time keeps increasing. These results clearly demonstrate the power boost associated with negative spin temperatures.

V. COMPARISON WITH AN N-LEVEL ENGINE

We next numerically compare the thermodynamic performance of our quasispin ($N = 7$)-level quantum heat engine to that of a ($N \leq 7$)-level machine in order to analyze the influence of the dimension of the Hilbert space
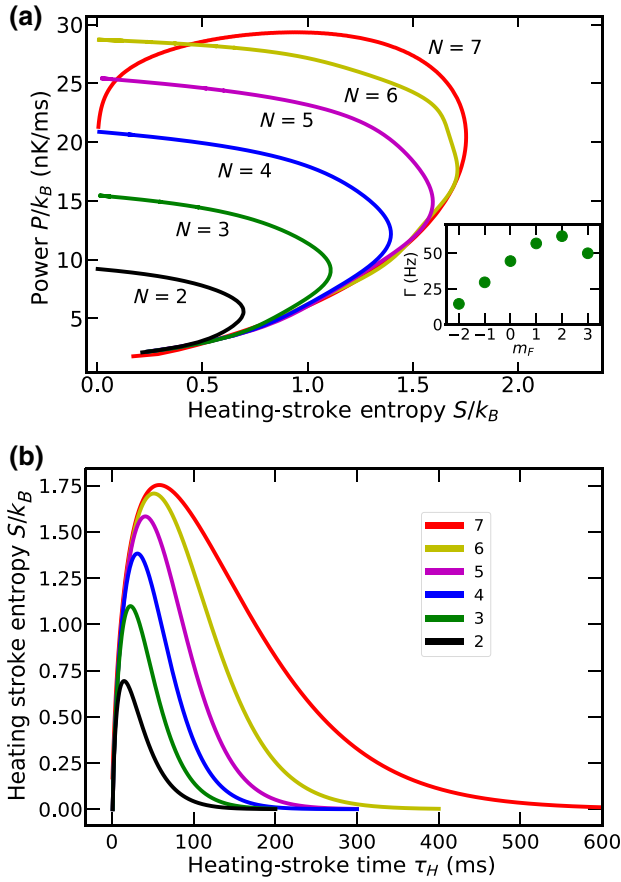
FIG. 5. (a) The evolution of the power output for a truncated working medium with $N \leq 7$ levels as a function of the heating-stroke Shannon entropy. The heat exchange rate and cycle time are considered to be the same as for the $(N = 7)$-level heat engine. The inset shows the rates between two neighboring levels during the heating stroke. The x axis gives the original state, i.e., $\Gamma^{3\rightarrow2}$, located at $m_{F,\mathrm{Cs}} = 3$, up to $\Gamma^{-2\rightarrow-3}$, located at $m_{F,\mathrm{Cs}} = -2$. (b) The evolution of the corresponding Shannon entropy as a function of the heating time τ_H.

on the power output and on the size of the quantum fluctuations in the system [61]. To that end, we simulate the behavior of the N-level system by truncating the system of rate equations that governs the evolution of the populations of the complete $N = 7$ system to a variable number $N \leq 7$, by keeping the transition rates unchanged [see Appendix A; in particular, Eq. (B1)]. For each system, $m_{F,\mathrm{Cs}} = 3$ continues to represent the ground state and the level spacing and environmental parameters are unchanged. This leads to systems with the same transition rates between neighboring states while the number of levels is reduced. Afterward, the corresponding heat exchange $Q_H = \sum_n E_n^{\mathrm{Cs}} \Delta p_n$ is determined from the spin dynamics. To guarantee the same heating velocity, the corresponding cycle time of the seven-level system is used for the same amount of exchanged heat.

Figure 5(a) shows the evolution of the power output, given in Eq. (3), as a function of the heating-stroke entropy for various numbers N of levels. We note that both the value of the maximum entropy and of the maximum power output increase with the number N of levels. A $(N \geq 2)$-level quantum heat engine thus outperforms a two-level machine (while displaying, at the same time, larger quantum fluctuations). Figure 5(b) shows the evolution of the corresponding Shannon entropy, given in Eq. (2). All N-level systems start with low power and entropy values. Both quantities increase until an entropy peak is reached. After peaking, higher-energy states are populated until the population is completely localized in the highest-energy state, corresponding to maximum engine-spin polarization, and the entropy decreases, ideally to zero. At the same time, the power is steadily increasing. Interestingly, we observe the same behavior for all reduced-level systems. The seven-level system overall shows the same behavior but for the last part of the evolution, the power drops slightly as the entropy decreases further. We attribute this small power drop to larger cycle times due to the low rate $\Gamma^{-2\rightarrow-3}$ that populates the $m_{F,\mathrm{Cs}} = -3$ state, as shown in the inset.

While the experimental analysis of Ref. [18] has been mostly focused on the efficiency increase of a two-level quantum Otto cycle associated with negative effective temperatures, our study reveals the remarkable advantage of using a multilevel working medium to achieve a significant power-output boost (of more than 200% between $N = 2$ and $N = 7$) at constant efficiency.

VI. CONCLUSIONS

We experimentally investigate the performance of a quasispin quantum Otto engine coupled to a quantum Rb bath in the regime of effective negative temperature. By employing time-resolved population measurements of the quasispin Cs state, we concretely examine the influence of the bounded discrete energy spectrum on both the effective spin temperature and the quantum fluctuations in the engine (quantified with the Shannon entropy), during the entire thermodynamic cycle. We observe the transition to negative effective temperatures when the Shannon entropy of the quasispin distribution reaches its maximal value (after six spin-exchange collisions), corresponding to maximum quantum fluctuations. We additionally find that the power output is maximal at half the maximum entropy (after 11 spin-exchange collisions). Overall, negative spin temperatures lead to a significant increase of the power output of the engine, up to 30% compared to positive spin temperatures for the parameters of our experiment. Additionally, the natural interaction stop, with its polarizing effect in the outmost states, halves the entropy with respect to its peak value while the engine provides maximum power output. Our findings offer insight into the

connection between the dynamics of quantum spin populations of a multilevel heat engine and its thermodynamic properties at the level of individual quanta.

APPENDIX A: TEMPERATURE FIT

During the heating and cooling strokes, the Cs population can be inverted, i.e., the majority is populating energetically lower or higher states. The heating stroke
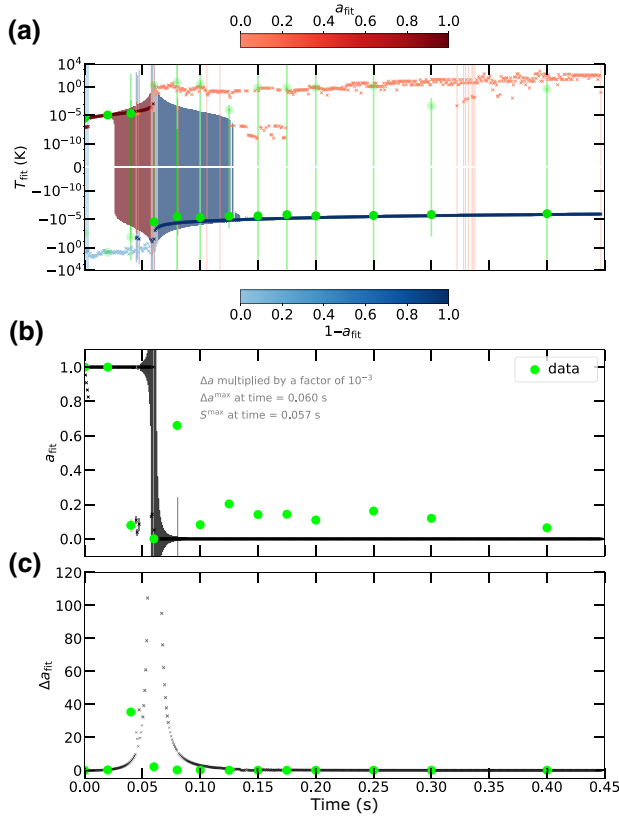

FIG. 6. The Cs population fitted by a combination of Boltzmann distributions with negative and positive temperatures. (a) The fitted temperature over the heating time. Our engine shows a thermal behavior for short times until it reaches the transition from positive to negative temperature at roughly 60 ms, corresponding to maximum entropy. Further away from this area, the system can be described by an almost exclusively positive (negative) temperature for short (long) heating times. (b),(c) The fit parameter a (b) with its width Δa_{fit} (c). The green dots show data and the colored lines simulations.
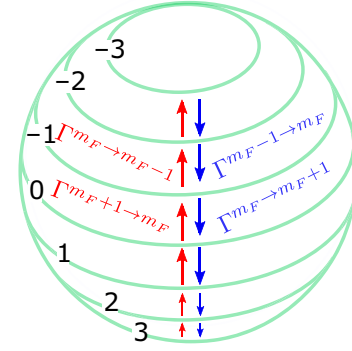

FIG. 7. An illustration of the Cs spin-exchange rate. The Bloch sphere illustrates the seven-level Cs spin system with corresponding $m_{F,\mathrm{Cs}}$ numbers. The red (blue) arrows present the rates between two neighboring states for the heating (cooling) stroke.

starts in the ground state, $|m_{F,\mathrm{Cs}} = 3\rangle$, and is populating energetically higher states. To extract the temperature of the Cs spin population, we use a combination of two Boltzman distributions with positive and negative temperatures, respectively. The fitted population is written as $P_n = aP_+ + (1 - a)P_-$, where $P_{\pm} = \exp(-E_n^{\mathrm{Cs}}/k_B T_{\pm})/Z_{\pm}$, with the partition function $Z_{\pm}$, and with positive (T_+) and negative (T_-) temperatures. The fit parameter a gives the contribution of each temperature regime. Figure 6(a) shows the two temperature regimes for different heating times with the transition to negative temperatures. The color code represents the weighted influence of each temperature regime. This transition is also evident when considering the behavior of the fit parameter a [Fig. 6(b)] and the corresponding width Δa [Fig. 6(c)]. The green dots show data and the colored lines simulations based on our spin-exchange model (see Appendix B).

APPENDIX B: SPIN-EXCHANGE MODEL

To model the seven-level Cs system, we simulate the spin dynamics using a rate equation, given in Eq. (B1). The vector P_{m_F} gives the population. The transition rates between two neighboring states are presented as a matrix (B1)

$$\dot{P}_{m_F} = \begin{pmatrix} 0 & -\Gamma^{m_F \to m_F+1} & 0 & \\ \Gamma^{m_F+1 \to m_F} & 0 & \Gamma^{m_F-1 \to m_F} & \\ 0 & -\Gamma^{m_F \to m_F-1} & 0 & \cdots \\ & & \vdots & \end{pmatrix}$$

$$\cdot \begin{pmatrix} P_{m_F+1} \\ P_{m_F} \\ P_{m_F-1} \\ \vdots \end{pmatrix}. \quad (B1)$$

Each rate is calculable as [13]

$$\Gamma^{m_F} = \langle n \rangle\, \sigma_{m_F}\, \bar{v}. \quad (B2)$$

Here, σ_{m_F} gives the cross section, $\langle n \rangle = \int n_{Cs}(\vec{r}) \, n_{Rb}(\vec{r}) \, d\vec{r}$ is the density overlap between the two atomic species, and $\bar{v} = [(8 \, k_B \, T)/(\pi \, \mu)]^{1/2}$ is the relative velocity with reduced mass μ. Figure 7 shows the seven-level system with corresponding transition rates. For the cooling (heating) stroke, the bath polarizes the $|m_{F,Rb}\rangle = 1$ ($|m_{F,Rb}\rangle = -1$) state. Processes that populate higher (lower) energetic Cs states are energetically forbidden, i.e., the red (blue) indicated rates are negligible.

---

[1] Y. A. Cengel and M. A. Boles, *Thermodynamics: An Engineering Approach* (McGraw-Hill, New York, 2001).

[2] T. Hugel, N. B. Holland, A. Cattani, L. Moroder, M. Seitz, and H. E. Gaub, Single-Molecule Optomechanical Cycle, Science **296**, 1103 (2002).

[3] P. G. Steeneken, K. Le Phan, M. J. Goossens, G. E. J. Koops, G. J. A. M. Brom, C. van der Avoort, and J. T. M. van Beek, Piezoresistive heat engine and refrigerator, Nature Phys. **7**, 354 (2011).

[4] V. Blickle and C. Bechinger, Realization of a micrometre-sized stochastic heat engine, Nature Phys. **8**, 143 (2012).

[5] P. Quinto-Su, A microscopic steam engine implemented in an optical tweezer, Nat. Commun. **5**, 5889 (2014).

[6] I. A. Martinez, E. Roldan, L. Dinis, D. Petrov, J. M. R. Parrondo, and R. A. Rica, Brownian Carnot engine, Nat. Phys. **12**, 67 (2015).

[7] J. Rossnagel, S. T. Dawkins, K. N. Tolazzi, O. Abah, E. Lutz, F. Schmidt-Kaler, and K. Singer, A single-atom heat engine, Science **352**, 325 (2016).

[8] D. von Lindenfels, O. Grab, C. T. Schmiegelow, V. Kaushal, J. Schulz, M. T. Mitchison, J. Goold, F. Schmidt-Kaler, and U. G. Poschinger, Spin Heat Engine Coupled to a Harmonic-Oscillator Flywheel, Phys. Rev. Lett. **123**, 080602 (2019).

[9] N. Van Horne, D. Yum, T. Dutta, P. Hänggi, J. Gong, D. Poletti, and M. Mukherjee, Single-atom energy-conversion device with a quantum load, npj Quantum Inf. **6**, 37 (2020).

[10] Y. Zou, Y. Jiang, Y. Mei, X. Guo, and S. Du, Quantum Heat Engine Using Electromagnetically Induced Transparency, Phys. Rev. Lett. **119**, 050602 (2017).

[11] J. Klatzow, J. Becker, P. Ledingham, C. Weinzetl, K. Kaczmarek, D. Saunders, J. Nunn, I. Walmsley, R. Uzdin, and E. Poem, Experimental Demonstration of Quantum Effects in the Operation of Microscopic Heat Engines, Phys. Rev. Lett. **122**, 110601 (2019).

[12] J. P. S. Peterson, T. B. Batalhão, M. Herrera, A. M. Souza, R. S. Sarthour, I. S. Oliveira, and R. M. Serra, Experimental Characterization of a Spin Quantum Heat Engine, Phys. Rev. Lett. **123**, 240601 (2019).

[13] Q. Bouton, J. Nettersheim, S. Burgardt, D. Adam, E. Lutz, and A. Widera, A quantum heat engine driven by atomic collisions, Nat. Commun. **12**, 2063 (2021).

[14] M. O. Scully, M. S. Zubairy, G. Agarwal, and H. Walther, Extracting Work from a Single Heat Bath via Vanishing Quantum Coherence, Science **299**, 862 (2003).

[15] M. O. Scully, K. R. Chapin, K. E. Dorfman, M. B. Kim, and Svidzinsky, Quantum heat engine power can be increased by noise-induced coherence, Proc. Natl. Acad. Sci. USA **108**, 15097 (2011).

[16] J. Rossnagel, O. Abah, F. Schmidt-Kaler, K. Singer, and E. Lutz, Nanoscale Heat Engine beyond the Carnot Limit, Phys. Rev. Lett. **112**, 03602 (2014).

[17] J. Klaers, S. Faelt, A. Imamoglu, and E. Togan, Squeezed Thermal Reservoirs as a Resource for a Nanomechanical Engine beyond the Carnot Limit, Phys. Rev. X **7**, 031044 (2017).

[18] R. J. de Assis, T. M. de Mendonca, C. J. Villas-Boas, A. M. de Souza, R. S. Sarthour, I. S. Oliveira, and N. G. de Almeida, Efficiency of a Quantum Otto Heat Engine Operating under a Reservoir at Effective Negative Temperatures, Phys. Rev. Lett. **122**, 240602 (2019).

[19] O. Abah and E. Lutz, Efficiency of heat engines coupled to nonequilibrium reservoirs, EPL **106**, 20001 (2014).

[20] R. Alicki and D. Gelbwaser-Klimovsky, Non-equilibrium quantum heat machines, New J. Phys. **17**, 115012 (2015).

[21] E. M. Purcell and R. V. Pound, A Nuclear Spin System at Negative Temperature, Phys. Rev. **81**, 279 (1951).

[22] A. S. Oja and O. V. Lounasmaa, Nuclear magnetic ordering in simple metals at positive and negative nanokelvin temperatures, Rev. Mod. Phys. **69**, 1 (1997).

[23] P. Medley, D. M. Weld, H. Miyake, D. E. Pritchard, and W. Ketterle, Spin Gradient Demagnetization Cooling of Ultracold Atoms, Phys. Rev. Lett. **106**, 195301 (2011).

[24] S. Braun, J. P. Ronzheimer, M. Schreiber, S. S. Hodgman, T. Rom, I. Bloch, and U. Schneider, Negative Absolute Temperature for Motional Degrees of Freedom, Science **339**, 52 (2013).

[25] N. F. Ramsey, Thermodynamics and Statistical Mechanics at Negative Absolute Temperatures, Phys. Rev. **103**, 20 (1956).

[26] J. Lielmezs and W. D. Groves, Negative Temperatures, Nature **210**, 723 (1966).

[27] P. Ehrlich, Negative, infinite, and hotter than infinite temperatures, Synthese **50**, 233 (1982).

[28] A. P. Mosk, Atomic Gases at Negative Kinetic Temperature, Phys. Rev. Lett. **95**, 040403 (2005).

[29] A. Rapp, S. Mandt, and A. Rosch, Equilibration Rates and Negative Absolute Temperatures for Ultracold Atoms in Optical Lattices, Phys. Rev. Lett. **105**, 220405 (2010).

[30] J. Dunkel and S. Hilbert, Consistent thermostatistics forbids negative absolute temperatures, Nature Phys. **10**, 67 (2014).

[31] H. Struchtrup, Work Storage in States of Apparent Negative Thermodynamic Temperature, Phys. Rev. Lett. **120**, 250602 (2018).

[32] Y. Hama, W. J. Munro, and K. Nemoto, Relaxation to Negative Temperatures in Double Domain Systems, Phys. Rev. Lett. **120**, 060403 (2018).

[33] M. Baldovin, S. Iubini, R. Livi, and A. Vulpiani, Statistical mechanics of systems with negative temperature, Phys. Rep. **923**, 1 (2021).

[34] M. O. Scully and M. S. Zubairy, *Quantum Optics* (Cambridge University Press, Cambridge, 1997).

[35] C. Kittel and H. Kroemer, *Thermal Physics* (Freeman, New York, 1980).

[36] P. T. Landsberg, Heat engines and heat pumps at positive and negative absolute temperatures, J. Phys. A: Math. Gen. **10**, 1773 (1977).

[37] P. T. Landsberg, R. J. Tykodi, and A. M. Tremblay, Systematics of Carnot cycles at positive and negative kelvin temperatures, J. Phys. A: Math. Gen. **13**, 1063 (1980).

[38] T. Nakagomi, Mathematical formulation of the heat-engine theory of thermodynamics including negative absolute temperatures, J. Phys. A: Math. Gen. **14**, 2175 (1981).

[39] N. Brunner, N. Linden, S. Popescu, and P. Skrzypczyk, Virtual qubits, virtual temperatures, and the foundations of thermodynamics, Phys. Rev. E **85**, 051117 (2012).

[40] J.-Y. Xi and H.-T. Quan, Quantum Heat Engine and Negative Boltzmann Temperature, Commun. Theor. Phys. **68**, 347 (2017).

[41] N. V. Prokof'ev and P. C. E. Stamp, Theory of the spin bath, Rep. Prog. Phys. **63**, 669 (2000).

[42] J. Fischer and H.-P. Breuer, Correlated projection operator approach to non-Markovian dynamics in spin baths, Phys. Rev. A **76**, 052119 (2007).

[43] Y. Hamdouni and F. Petruccione, Time evolution and decoherence of a spin-12 particle coupled to a spin bath in thermal equilibrium, Phys. Rev. B **76**, 174306 (2007).

[44] E. Ferraro, H.-P. Breuer, A. Napoli, M. A. Jivulescu, and A. Messina, Non-Markovian dynamics of a single electron spin coupled to a nuclear spin bath, Phys. Rev. B **78**, 064309 (2008).

[45] E. Barnes, L. Cywinski, and S. Das Sarma, Nonperturbative Master Equation Solution of Central Spin Dephasing Dynamics, Phys. Rev. Lett. **109**, 140403 (2012).

[46] V. Semin, I. Sinayskiy, and F. Petruccione, Arbitrary spin in a spin bath: Exact dynamics and approximation techniques, Phys. Rev. A **89**, 012107 (2014).

[47] C. Mukhopadhyay, S. Bhattacharya, A. Misra, and A. K. Pati, Dynamics and thermodynamics of a central spin immersed in a spin bath, Phys. Rev. A **96**, 052125 (2017).

[48] S. Bhattacharya, A. Misra, C. Mukhopadhyay, and A. K. Pati, Exact master equation for a spin interacting with a spin bath: Non-Markovianity and negative entropy production rate, Phys. Rev. A **95**, 012122 (2017).

[49] J. S. S. T. Wright, T. Gould, A. R. R. Carvalho, S. Bedkihal, and J. A. Vaccaro, Quantum heat engine operating between thermal and spin reservoirs, Phys. Rev. A **97**, 052104 (2018).

[50] C. Mukhopadhyay, Generating steady quantum coherence and magic through an autonomous thermodynamic machine by utilizing a spin bath, Phys. Rev. A **98**, 012102 (2018).

[51] D. Segal, Two-level system in spin baths: Non-adiabatic dynamics and heat transport, J. Chem. Phys. **140**, 164110 (2014).

[52] G. Katz and R. Kosloff, Quantum Thermodynamics in Strong Coupling: Heat Transport and Refrigeration, Entropy **18**, 186 (2016).

[53] F. Ciccarello, S. Lorenzo, V. Giovannetti, and G. M. Palma, Quantum collision models: Open system dynamics from repeated interactions, Phys. Rep. **954**, 1 (2022).

[54] R. Kosloff and Y. Rezek, The Quantum Harmonic Otto Cycle, Entropy **19**, 136 (2017).

[55] F. Schmidt, D. Mayer, Q. Bouton, D. Adam, T. Lausch, J. Nettersheim, E. Tiemann, and A. Widera, Tailored Single-Atom Collisions at Ultra-Low Energies, Phys. Rev. Lett. **122**, 013401 (2019).

[56] T. Sikorsky, Z. Meir, R. Ben-shlomi, N. Akerman, and R. Ozeri, Spin-controlled atom-ion chemistry, Nat. Commun. **9**, 920 (2018).

[57] Q. Bouton, J. Nettersheim, D. Adam, F. Schmidt, D. Mayer, T. Lausch, E. Tiemann, and A. Widera, Single-Atom Quantum Probes for Ultracold Gases Boosted by Nonequilibrium Spin Dynamics, Phys. Rev. X **10**, 011018 (2020).

[58] H. Maassen and J. B. M. Uffink, Generalized Entropic Uncertainty Relations, Phys. Rev. Lett. **60**, 1103 (1988).

[59] P. J. Coles, R. Colbeck, L. Yu, and M. Zwolak, Uncertainty Relations from Simple Entropic Properties, Phys. Rev. Lett. **108**, 210405 (2012).

[60] P. J. Coles, M. Berta, M. Tomamichel, and S. Wehner, Entropic uncertainty relations and their applications, Rev. Mod. Phys. **89**, 015002 (2017).

[61] T. Denzler and E. Lutz, Power fluctuations in a finite-time quantum Carnot engine, Phys. Rev. Res. **3**, L032041 (2021).